Terr. Atmos. Ocean. Sci., Vol. 24, No. 5, 793-807, October 2013 doi: 10.3319/TAO.2013.05.08.01(T)

Effect of Crustal Density Structures on GOCE Gravity Gradient Observables

Robert Tenzer[1, *] and Pavel Novák[2]

[1] *School of Geodesy and Geomatics, Wuhan University, Wuhan, China*
[2] *New Technologies for the Information Society (NTIS), Faculty of Applied Sciences, University of West Bohemia, Plzen, Czech Republic*

Received 3 December 2012, accepted 8 May 2013

ABSTRACT

We investigate the gravity gradient components corrected for major known anomalous density structures within the Earth's crust. Heterogeneous mantle density structures are disregarded. The gravimetric forward modeling technique is utilized to compute the gravity gradients based on methods for a spherical harmonic analysis and synthesis of a gravity field. The Earth's gravity gradient components are generated using the global geopotential model GOCO-03s. The topographic and stripping gravity corrections due to the density contrasts of the ocean and ice are computed from the global topographic/bathymetric model DTM2006.0 (which also includes the ice-thickness dataset). The discrete data of sediments and crust layers taken from the CRUST2.0 global crustal model are then used to apply the additional stripping corrections for sediments and remaining anomalous crustal density structures. All computations are realized globally on a one arc-deg geographical grid at a mean satellite elevation of 255 km. The global map of the consolidated crust-stripped gravity gradients reveals distinctive features which are attributed to global tectonics, lithospheric plate configuration, lithosphere structure and mantle dynamics (e.g., glacial isostatic adjustment, mantle convection). The Moho signature, which is the most pronounced signal in these refined gravity gradients, is superimposed over a weaker gravity signal of the lithospheric mantle. An interpretational quality of the computed (refined) gravity gradient components is mainly limited by a low accuracy and resolution of the CRUST2.0 sediment and crustal layer data and unmodeled mantle structures.

Key words: Crust, Forward modeling, GOCE, Gravity Gradiometry, Mantle

Citation: Tenzer, R. and P. Novák, 2013: Effect of crustal density structures on GOCE gravity gradient observables. Terr. Atmos. Ocean. Sci., 24, 793-807, doi: 10.3319/TAO.2013.05.08.01(T)

1. INTRODUCTION

When studying the Moho density interface based on gravity field analysis and inversion, the topographic, bathymetric and additional corrections which account for anomalous mass density structures within the Earth's crust are applied to observed gravity data (see e.g., Sjöberg and Bagherbandi 2011; Sampietro et al. 2013). In geophysics, this step is known as gravity stripping (e.g., Hammer 1963). In addition to modeling of crustal density structures, the gravity signal of heterogeneous density structures within the lithospheric mantle as well as deeper mantle (including core-mantle geometry) should be modeled and subsequently removed from these refined gravity data. In this study, we take into consideration only major density structures within the Earth's crust; heterogeneous mantle density structures are disregarded. The 3-D global model of the mantle density distribution was compiled, for instance, by Simmons et al. (2010). There are several different geophysical phenomena (such as glacial isostatic adjustment, plate flexure, crustal rigidity, plate motion, mantle convection/thermal compensation) which can also be interpreted by means of gravity field analysis. For more information we refer readers to studies by Kaban et al. (1999, 2003, 2004), Watts (2001, p. 114), Braitenberg et al. (2006), Wienecke et al. (2007), Tenzer et al. (2009a, 2012b), Bagherbandi and Sjöberg (2012), Negretti et al. (2012), and others.

In association with the precise modeling of the Earth's gravity field, three dedicated satellite missions provide information which considerably increased the accuracy of existing global geopotential models (GGMs) and significantly

* *Corresponding author*
E-mail: rtenzer@sgg.whu.edu.cn

improved their application in various scientific fields: the CHAllenging Mini-satellite Payload (CHAMP) launched in 2000, the GRavity field and Climate Experiment (GRACE) launched in 2002, and the Gravity field and steady-state Ocean Circulation Explorer (GOCE) launched in 2009. These missions are somewhat complementary. The GOCE gravity gradiometry significantly improved the gravity field at medium wavelengths from about 100 to 250 of spherical harmonics (and provides a spatial resolution to about 70 km at the equator), but it is relatively inaccurate at long wavelengths (above 700 - 1000 km). The CHAMP and GRACE missions provide precise information on a long-wavelength gravity spectrum up to degree of 160 (which correspond to a spatial resolution of about 200 km at the equator). An assessment of the accuracy of recent combined satellite models can be found, for instance in Pail et al. (2007) and Förste et al. (2008). The combined CHAMP/GRACE/GOCE gravity field solutions have the ability to extend current knowledge concerning the Earth's inner density structures especially beneath oceanic and continental areas where seismic data are not yet available or their accuracy and spatial coverage is inadequate.

In this study we use the recently released model GOCO-03s (Mayer-Gürr et al. 2012) to compute the gravity gradient components globally. This model was compiled based upon GOCE, GRACE, CHAMP and SLR (Satellite Laser Ranging) observations, and is effective to a maximum degree of 250 of spherical harmonics. The computations are conducted for the diagonal components of the Marussi gravity gradient tensor defined in the geocentric system of spherical coordinates. We then apply topographic and crustal components stripping corrections to the GOCO-03s gravity gradients in order to present and interpret the signature of the Moho geometry and other mainly lithospheric structural compositions in the (refined) gravity gradient field. We expect to achieve a more detailed interpretational quality (for instance, contrast between the oceanic and continental crustal structures) when using the gravity gradient field instead of gravity or potential fields.

2. METHODOLOGY

The expressions for the gravimetric forward modeling reviewed in Appendices A and B were utilized to compute topographic and stripping gravity gradient corrections due to density contrasts of the ocean, ice, sediments and within consolidated (crystalline) crust. These corrections were then applied to gravity gradient components. All computations were incorporated globally on a one arc-deg spherical coordinate grid at a mean satellite elevation of 255 km. The gravity gradient components were generated using the GOCO-03s coefficients with a spectral resolution complete to degree of 180 of spherical harmonics (which corresponds to a half-wavelength of one arc-deg or about 100 km at the equator). The spherical harmonic terms of the normal gravity field were computed according to the parameters of GRS-80 (Moritz 2000).

The topographic and bathymetric stripping (ocean density contrast) gravity gradient corrections were calculated with a spherical resolution complete to degree of 180 of spherical harmonics. Both corrections were computed using the DTM2006.0 coefficients (Pavlis et al. 2012). The global topographic/bathymetric model DTM2006.0 was released together with EGM2008 (Pavlis et al. 2012) by the US National Geospatial-Intelligence Agency EGM development team. An average density of the upper continental crust of 2670 kg m^{-3} (Hinze 2003) was adopted for defining topographic and reference crustal densities. The bathymetric stripping gravity gradient correction was computed utilizing a depth-dependent seawater density model (Tenzer et al. 2012c). This empirical ocean density model was developed by Gladkikh and Tenzer (2012) based on an analysis of oceanographic data of the World Ocean Atlas 2009 (WOA09) and the World Ocean Circulation Experiment 2004 (WOCE04). WOA09 oceanographic products are made available by NOAA's National Oceanographic Data Center (Johnson et al. 2009). The WOCE04 datasets are provided by the German Federal Maritime and Hydrographic Agency (Gouretski and Koltermann 2004). Tenzer et al. (2011) showed, based on a comparison of experimental and theoretical seawater density values, that this empirical model approximates the actual seawater density distribution with a maximum relative error of 0.6%; the corresponding average error is about 0.1%. For the adopted values of the reference crustal density (2670 kg m^{-3}) and surface seawater density (1028 kg m^{-3}) (Gladkikh and Tenzer 2012), the nominal ocean density contrast (at zero depth) equals 1642 kg m^{-3}. The parameters of the depth-dependent ocean density term in Eq. (A8) are: $\beta = 0.00637$ kg m^{-3}, $a_1 = 0.7595$ m^{-1}, and $a_2 = -4.3984 \times 10^{-6}$ m^{-2} (Tenzer et al. 2012c).

The 5 × 5 arc-minutes grid of continental ice-thickness values from the DTM2006.0 dataset was used to generate the coefficients of a global ice-thickness model. These grid data were derived from the Kort and Matrikelstyrelsen (KMS) ice-thickness data for Greenland (Ekholm 1996) and from updated ice-thickness data for Antarctica assembled by the BEDMAP project (Lythe and Vaughan 2001). The ice-thickness coefficients combined with the DTM2006.0 topographic coefficients were then used to compute the ice stripping gravity gradient correction with a spectral resolution complete to degree of 180. For the adopted values of the reference crustal density (2670 kg m^{-3}) and the density of glacial ice (917 kg m^{-3}) (Cutnell and Kenneth 1995), the ice density contrast is 1753 kg m^{-3} (Tenzer et al. 2010).

The 2 × 2 arc-deg global data of the soft and hard sediment depth, thickness and density from CRUST2.0 (Bassin et al. 2000) were used to generate the coefficients of the global sediment model. This model was compiled and

administered by the US Geological Survey and the Institute for Geophysics and Planetary Physics at the University of California. The sediment stripping gravity gradient correction was computed with a spectral resolution complete to degree of 90. This spatial resolution is compatible with a 2 × 2 arc-deg spatial resolution of CRUST2.0. The CRUST2.0 soft sediments vary in density from 1700 to 2300 kg m^{-3} and reach a maximum thickness of about 2 km, while the CRUST2.0 hard sediments vary in density between 2300 and 2600 kg m^{-3} and reach the maximum thickness of 18 km. The sediment density contrast was taken relative to the reference crustal density of 2670 kg m^{-3}.

The 2 × 2 arc-deg global thickness, depth and density data of the upper, middle and lower consolidated crust from CRUST2.0 were used to generate the coefficients which describe the geometry and density distributions within these three (consolidated) crustal layers. The respective crust-stripping gravity gradient correction was then computed with a spectral resolution complete to degree of 90. The crustal density contrast was again taken relative to the reference crustal density of 2670 kg m^{-3}. The range of lateral densities within the three crustal layers of CRUST2.0 is between 2600 and 3100 kg m^{-3}.

3. RESULTS

The global maps of the gravity gradient components Γ_{rr}, $\Gamma_{\phi\phi}$ and $\Gamma_{\lambda\lambda}$ computed on a one arc-deg grid at a mean satellite elevation of 255 km are shown in Fig. 1. The corresponding stepwise corrected gravity gradient components are shown in Figs. 2 - 6. The statistics of the results are summarized in Table 1.

4. ERROR ANALYSIS

The accuracy of the consolidated crust-stripped gravity gradient components depends on the errors of models used and the approximations in applied numerical schemes. The GOCO-03s gravity field quantities can be computed with relatively high accuracy. This is due to the fact that GOCE gravity gradient observations considerably increased the accuracy of current global gravity models at the medium-wavelength part of the gravity spectrum (to approximately between 100 to 250 degrees of spherical harmonics; e.g., Goiginger et al. 2001). Similarly, currently available global bathymetric, topographic and ice-thickness models are provided with relatively high accuracy and resolution. The largest errors in computed values of the topographic gravity correction are due to the absence of reliable data about the actual topographic density distribution. These density uncertainties can cause large errors especially over mountainous regions with variable geological structures. The approximation of the actual topographic density distribution by its mean value can yield local errors of 10% or more in computed values of the topographic stripping correction, provided that the density errors propagate proportionally to the gravity gradient uncertainties. This relative error corresponds to uncertainties of about 0.5 E in computed values of the vertical gravity gradients. The computation of the bathymetric stripping gravity gradient correction requires an accurate model of seawater density. When the actual seawater density is approximated by its mean value, relative inaccuracies up to about 2% were estimated in the computed values of the bathymetric stripping gravity correction (Tenzer et al. 2011). The errors in the bathymetric stripping gravity gradient correction can then reach as much as 0.1 E. Therefore, in this study we used a depth-dependent seawater density model in which average accuracy is better than 0.1%. The application of the additional stripping gravity correction, which accounts for major known anomalous crustal density structures, is also essential. The application of an ice stripping correction, for instance, significantly improved the interpretational quality of the gravity gradient field along the continental margins of Greenland and Antarctica. We anticipate large errors in computed gravity gradients due to inaccuracies within the CRUST2.0 sediments and consolidated crust layers. A realistic assessment of these errors is not simple. The CRUST2.0 sediment data consist of soft and hard sediment model components using a laterally varying density structure, but without taking fully into consideration the density increase with depth due to sediment compaction. An improvement in accuracy can then be expected when utilizing a depth-dependent sediment density model (e.g., Artemjev et al. 1994). An application of the final stripping correction due to anomalous density structures within the CRUST2.0 consolidated crust layers significantly changed the gravity gradient field (Table 1). Moreover, large parts of the globe are not yet sufficiently covered by seismic data (especially over oceans, Africa, Latin America and Antarctica). We thus expect that the largest errors are due to applying the consolidated crust-stripped gravity gradient correction.

5. DISCUSSION

The computed values of the Earth's radial gravity gradient component Γ_{rr} vary globally mostly within ±1.5 E (Fig. 1a). The corresponding horizontal gravity gradient components $\Gamma_{\phi\phi}$ and $\Gamma_{\lambda\lambda}$ have a range of values typically within ±1.0 E (Fig. 1b) and ±1.5 E (Fig. 1c), respectively. This range of gravity gradient values agrees with the fact that global spatial variations of the gravity disturbances are also within a relatively small interval of ±300 mGal (Tenzer et al. 2012b) and indicates that the Earth's lithosphere is almost completely in isostatic balance particularly at the long-wavelength segment of the gravity spectrum. The existing long-wavelength gravity signal is related mainly to deep mantle heterogeneities. Extreme values of gravity and corresponding spatial gravity changes apply mainly to mountainous regions

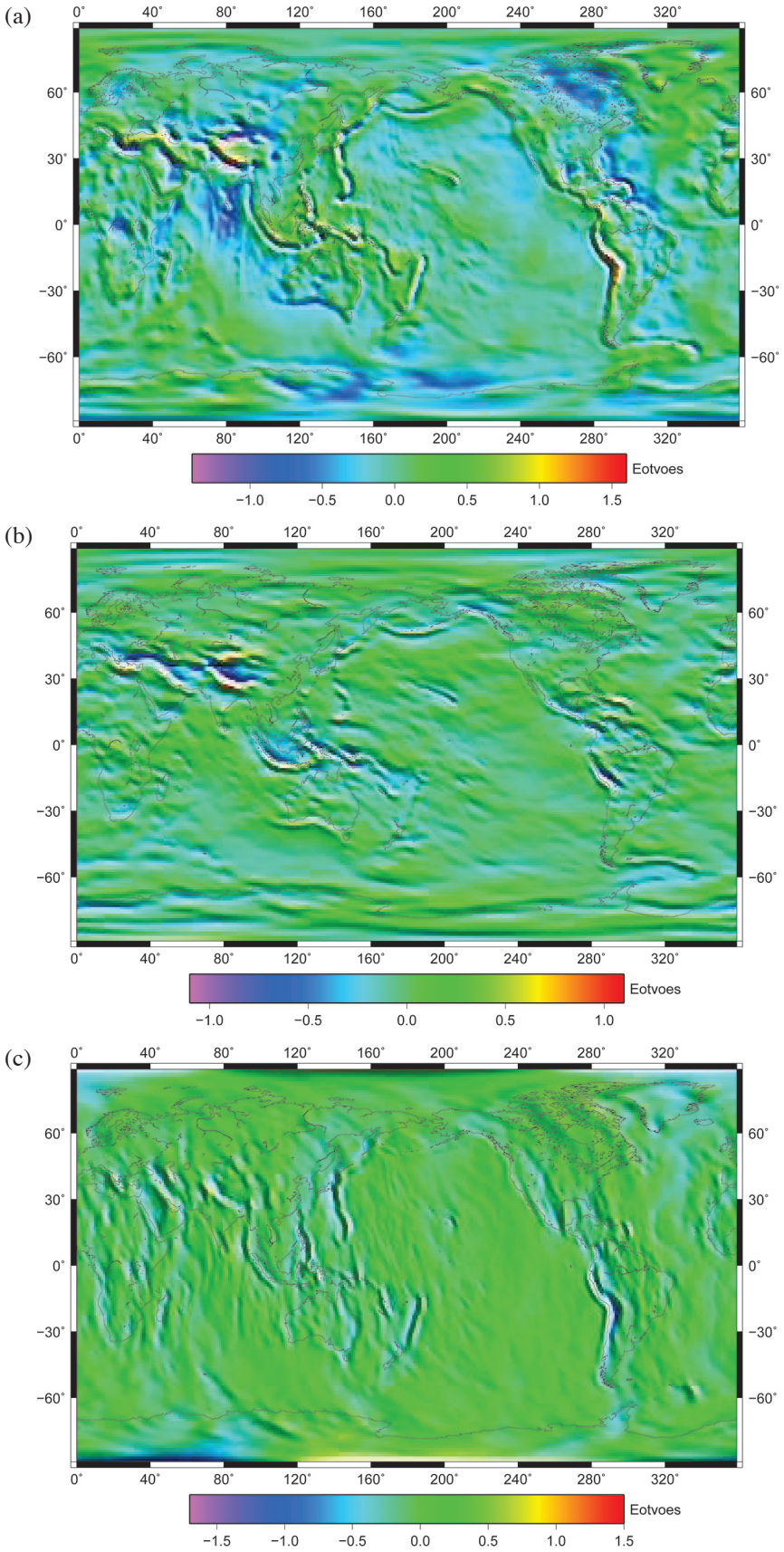

Fig. 1. The gravity gradient components: Γ_{rr} (a), $\Gamma_{\phi\phi}$ (b) and $\Gamma_{\lambda\lambda}$ (c) computed globally on a one arc-deg grid at a mean satellite elevation of 255 km using the GOCO-03s coefficients. Values are in E (= 10^{-9} s^{-2}).

Table 1. Statistics of the step-wise corrected gravity gradient components computed globally on a one arc-deg grid at a mean elevation of 255 km.

Gravity gradient quantity		Min [E]	Max [E]	Mean [E]	RMS [E]
GOCO-03s	Γ_{rr}	-1.40	1.62	0.00	0.24
	$\Gamma_{\phi\phi}$	-1.09	1.09	0.00	0.12
	$\Gamma_{\lambda\lambda}$	-1.65	1.43	0.00	0.17
Topography-corrected	Γ^{t}_{rr}	-6.09	1.16	-0.24	0.88
	$\Gamma^{t}_{\phi\phi}$	-1.89	3.94	-0.02	0.44
	$\Gamma^{t}_{\lambda\lambda}$	-2.52	3.55	0.00	0.43
Topography-corrected and bathymetry-stripped	Γ^{tb}_{rr}	-6.14	4.65	0.63	1.85
	$\Gamma^{tb}_{\phi\phi}$	-3.03	4.27	-0.02	0.89
	$\Gamma^{tb}_{\lambda\lambda}$	-3.51	5.43	0.00	0.86
Topography-corrected and bathymetry- and ice-stripped	Γ^{tbi}_{rr}	-6.14	4.65	0.72	1.62
	$\Gamma^{tbi}_{\phi\phi}$	-2.73	4.27	0.00	0.78
	$\Gamma^{tbi}_{\lambda\lambda}$	-2.79	5.43	0.00	0.77
Topography-corrected and bathymetry-, ice- and sediment-stripped	Γ^{tbis}_{rr}	-6.11	4.58	0.61	1.64
	$\Gamma^{tbis}_{\phi\phi}$	-2.85	3.94	0.00	0.78
	$\Gamma^{tbis}_{\lambda\lambda}$	-3.05	5.51	0.00	0.78
Consolidated crust-stripped	Γ^{cs}_{rr}	-2.72	4.63	1.57	0.94
	$\Gamma^{cs}_{\phi\phi}$	-1.66	2.22	-0.01	0.48
	$\Gamma^{cs}_{\lambda\lambda}$	-2.17	3.00	0.00	0.45

with large positive values of gravity disturbances and gravity gradients which have a predominantly high-frequency character; this gravity signal is highly correlated with the topography (Tenzer et al. 2009b). Corresponding negative values are detected along the oceanic subduction zones and continental basins. Long-wavelength anomalous features in the gravity gradient field are attributed to glacial isostatic adjustment as seen in Fennoscandia and Hudson Bay area. In contrast, the long-wavelength features attributed to heterogeneous mantle structures seen on the global map of the gravity disturbances (Tenzer et al. 2012b) are much less pronounced of the global gravity gradient field map (see Fig. 1a). The extreme values of the gravity gradient components Γ_{rr}, $\Gamma_{\phi\phi}$ and $\Gamma_{\lambda\lambda}$ obviously reflect the largest spatial gravity variations. The maxima of Γ_{rr} are found in the Himalayas and Andes and other mountainous regions. The extreme minima of Γ_{rr} are located along the continental basins. Geographically the largest area of negative gravity gradient values is located throughout the Hudson Bay. Over oceans, the areas of large negative values of Γ_{rr} correspond with the oceanic subduction zones. There we often see a coupling effect of these large negative values on the side of the subducted lithosphere with positive values on the other side of uplifted lithosphere. Moreover, the collision forces (along convergent tectonic zones) also result in positive values over areas behind the subducted lithosphere. We explain the presence of positive values at these locations by the plate flexure. The extreme values of the horizontal gravity gradient components $\Gamma_{\phi\phi}$ and $\Gamma_{\lambda\lambda}$ correspond with the largest spatial gravity changes in the meridional (for $\Gamma_{\phi\phi}$) and prime-vertical (for $\Gamma_{\lambda\lambda}$) directions.

The topography-corrected gravity gradient components Γ^{t}_{rr}, $\Gamma^{t}_{\phi\phi}$ and $\Gamma^{t}_{\lambda\lambda}$ have a considerably larger range of values compared to uncorrected components (see Fig. 2). The application of the topographic correction to observed gravity yields large negative values of the topography-corrected gravity disturbances in mountainous regions. As consequence, the largest negative values of Γ^{t}_{rr} are seen in mountainous regions of the Tibet Plateau, Himalayas and Andes. Large negative values of Γ^{t}_{rr} are also found in Antarctica and Greenland. Whereas continental areas have positive as well as negative values of Γ^{t}_{rr}, oceanic areas are characterized primarily by their small positive values. The most pronounced features over oceanic areas, as seen in the global map of Γ^{t}_{rr} (see Fig. 2a), are related to oceanic subduction zones. The pattern of the horizontal gravity gradient components $\Gamma^{t}_{\phi\phi}$ and $\Gamma^{t}_{\lambda\lambda}$ is again related to the largest spatial changes of the topography-corrected gravity field in their respective coordinate directions. The global map of $\Gamma^{t}_{\phi\phi}$

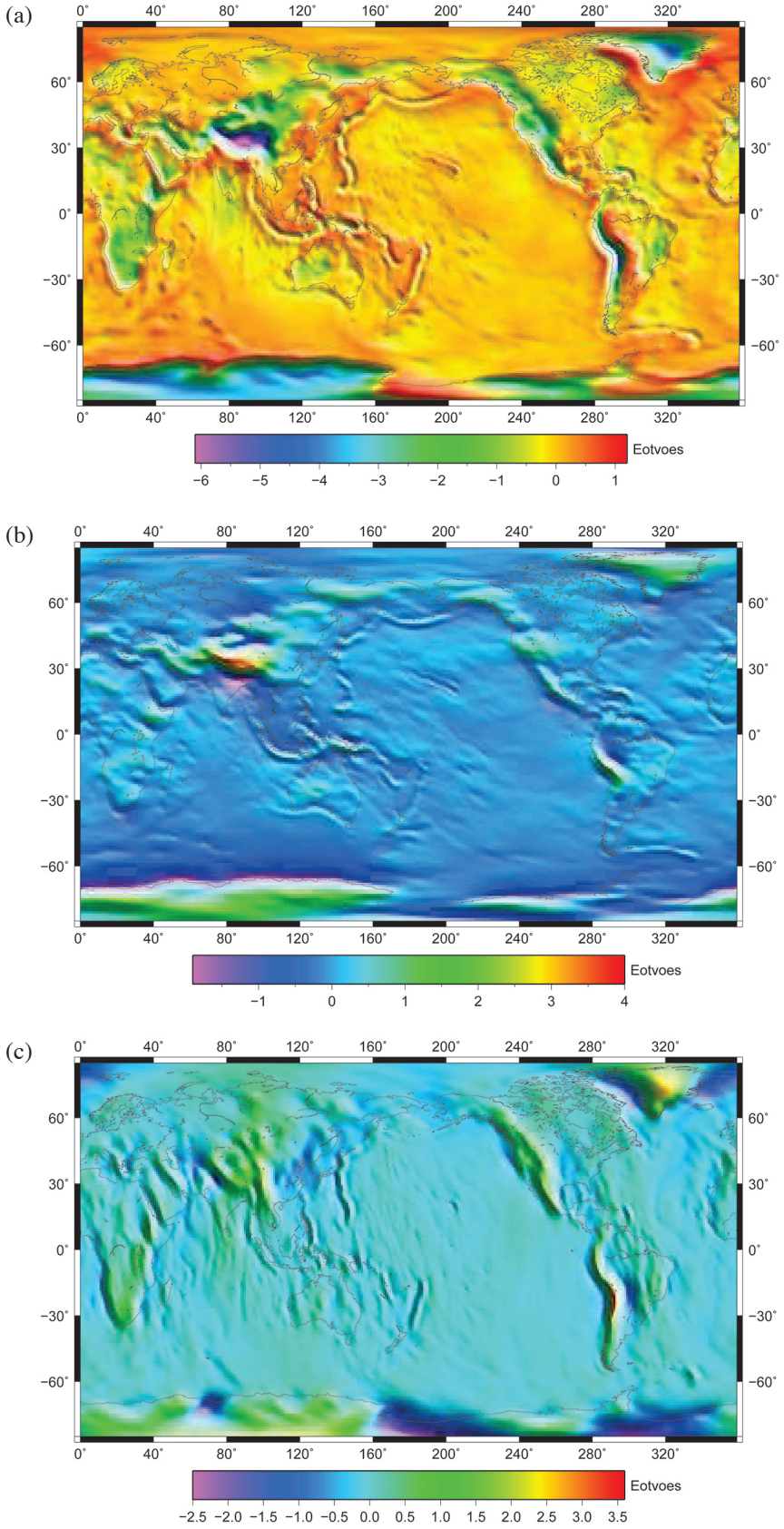

Fig. 2. The topography-corrected gravity gradient components: Γ^t_{rr}(a), $\Gamma^t_{\phi\phi}$(b) and $\Gamma^t_{\lambda\lambda}$(c) computed globally on a one arc-deg grid at a mean satellite elevation of 255 using the GOCO-03s and DTM2006 coefficients. Values are in E (= 10^{-9} s^{-2}).

revealed the signature of gravity changes along mountain chains with a prevailing parallel direction, and the map of $\Gamma^{t}_{\lambda\lambda}$ enhanced the pattern of spatial gravity variations across mountains and oceanic subduction zones with a prevailing meridional direction.

The application of the bathymetric stripping correction significantly changed the gravity field over oceans; the corresponding changes over continents have mostly a long-wavelength character (see Fig. 3). The largest positive values of Γ^{tb}_{rr} are detected along oceanic subduction zones. The absolute oceanic minima of Γ^{tb}_{rr} are situated along oceanic divergent tectonic plate boundaries (i.e., mid-oceanic ridges). These values increase slightly (in an absolute sense) towards the oceanic abyssal planes. The pattern of Γ^{tb}_{rr} over oceanic areas is thus significantly correlated with the geometry of the ocean bottom relief. The most pronounced feature in the map of Γ^{tb}_{rr} is the contrast between the oceanic and continental lithosphere along the continental margins. The meridional spatial variations of $\Gamma^{tb}_{\phi\phi}$ are again dominated by the contrast between the oceanic and continental lithosphere in a meridional direction, while the map of $\Gamma^{tb}_{\lambda\lambda}$ also shows the parallel gravity gradient variations over oceanic subduction zones. The horizontal gravity gradient components $\Gamma^{tb}_{\phi\phi}$ and $\Gamma^{tb}_{\lambda\lambda}$ are typically positive over continents while negative over oceans.

The application of the ice-stripping correction significantly changed the gravity gradient field in the polar areas of Antarctica and Greenland, especially along the margins of the continental ice sheets (Fig. 4a). The unrealistically large spatial variations of the gravity field in the polar areas are seen after applying the topographic correction computed for the topographic density of 2670 kg m^{-3} (Fig. 2a) and become considerably smaller. This is due to removing the gravitational signal of the continental ice sheet instead of subtracting an unrealistically large gravitational contribution of topography wherein the density is almost three times larger. The large negative values of Γ^{tb}_{rr} (to about -6 E) in the polar areas of Antarctica and Greenland (Fig. 3a) decreased (in an absolute sense) to less than -3 E for the values of Γ^{tbi}_{rr} (Fig. 4a). Similarly, the values of the corresponding horizontal components $\Gamma^{tbi}_{\phi\phi}$ and $\Gamma^{tbi}_{\lambda\lambda}$ now show a much less pronounced contrast along margins of the polar ice sheets (Figs. 4b and c) compared to the spatial variations of $\Gamma^{tb}_{\phi\phi}$ and $\Gamma^{tb}_{\lambda\lambda}$ (Figs. 3b and c) in their respective coordinate directions.

The application of the sediment-stripping correction does not significantly change the gravity gradient field (compare Figs. 4 and 5). These results agree with those of Tenzer et al. (2012b), who observed a similar effect when applying a sediment-stripping correction to gravity disturbances. The application of this correction only partially changed both gravity field quantities, especially over oceanic sedimentary basins and continental sediment deposits with the largest density contrasts. As a result, the contrast between oceanic and continental lithospheric structures was to some extent enhanced. A more detailed analysis also revealed that the most significant contribution to the gravity gradient field is due to CRUST2.0 soft sediments. This is explained by a larger density contrast and shallower locations of soft CRUST2.0 sediments. The statistics of sediment corrected and uncorrected gravity gradient components are very similar (Table 1).

The stripping correction due to the remaining anomalous density structures within the crustal layers significantly changed the gravity gradient field over certain areas of different crustal structures. As seen on the global map of the radial consolidated crust-stripped gravity gradient component Γ^{cs}_{rr} (Fig. 6a), the contrast between the continental and oceanic lithosphere was further enhanced. The most significant changes are observed in the Hudson Bay and Fennoscandia areas. There we see large positive values of Γ^{cs}_{rr} in Fennoscandia exceeding 4 E, while these values are typically below 2 E over the Hudson Bay. At both locations, the values of Γ^{cs}_{rr} increased substantially (up to about 2 E). We attribute these features to glacial isostatic adjustment. The application of the crust-stripping correction also changed the gravity gradient field considerably over North America revealing more detailed features of the North American Craton and the surrounding geological settings with sequences of platforms, shields, orogens and basins.

The continental as well as oceanic lithospheric structures are characterized by large spatial variations of the gravity gradient field with both positive and negative values (Fig. 6). The most pronounced features in the global map of Γ^{cs}_{rr} are related to the largest changes in the Moho geometry, especially under significant orogens and along the continental margins. Moreover, the signature of the divergent tectonic plate boundaries is clearly recognized along the mid-oceanic ridges as well as the continental rift zones (e.g., East African Rift, Red Sea, and West Antarctic Rift). These features are marked by negative values of Γ^{cs}_{rr}. Large negative values of Γ^{cs}_{rr} are detected over significant orogens (e.g., Tibet Plateau and Rocky Mountains) with the extreme minima in the surrounding continental basins (e.g., Tarim and Sichuan Basins). The contrast between the continental and oceanic lithospheric structures is typically marked by large positive values along oceanic subduction zones (e.g., Andes). In North America, the contrast between the North American Craton and oceanic lithosphere of the northern Atlantic Ocean is clearly marked by large negative values. The extreme maxima in are found in Fennoscandia. As discussed before, maxima Γ^{cs}_{rr} are related to glacial isostatic adjustment. The maps of the horizontal components $\Gamma^{cs}_{\phi\phi}$ and $\Gamma^{cs}_{\lambda\lambda}$ are complementary to the map of Γ^{cs}_{rr} showing in more detail the structures in particular coordinate directions.

6. SUMMARY AND CONCLUDING REMARKS

We have computed topographic and stripping gravity gradient corrections accounting for density contrasts of the

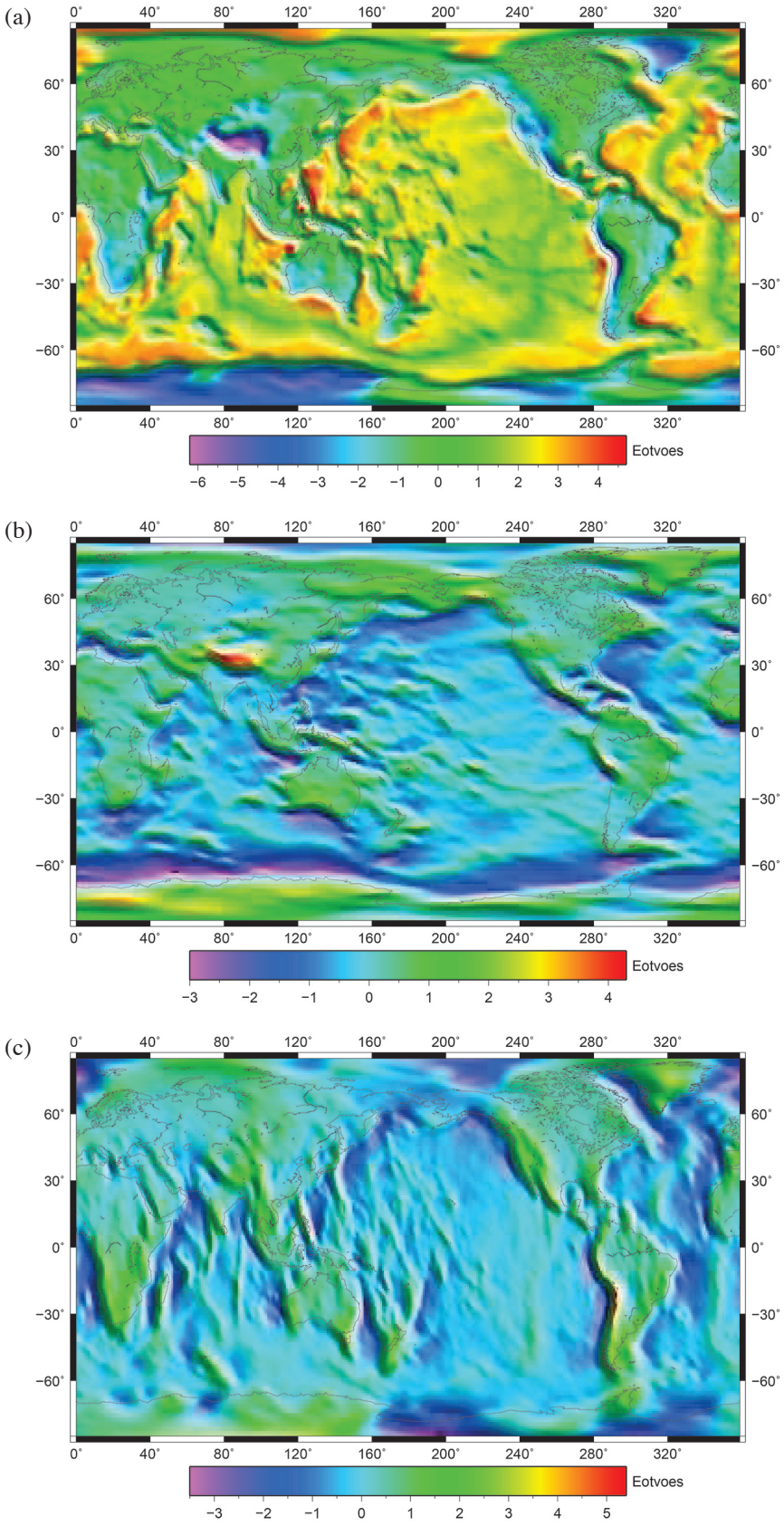

Fig. 3. The topography-corrected and bathymetry-stripped gravity gradient components: Γ_{rr}^{tb}(a), $\Gamma_{\phi\phi}^{tb}$(b) and $\Gamma_{\lambda\lambda}^{tb}$(c) computed globally on a one arc-deg grid at a mean satellite elevation of 255 km using the GOCO-03s and DTM2006 coefficients. Values are in E (= 10^{-9} s^{-2}).

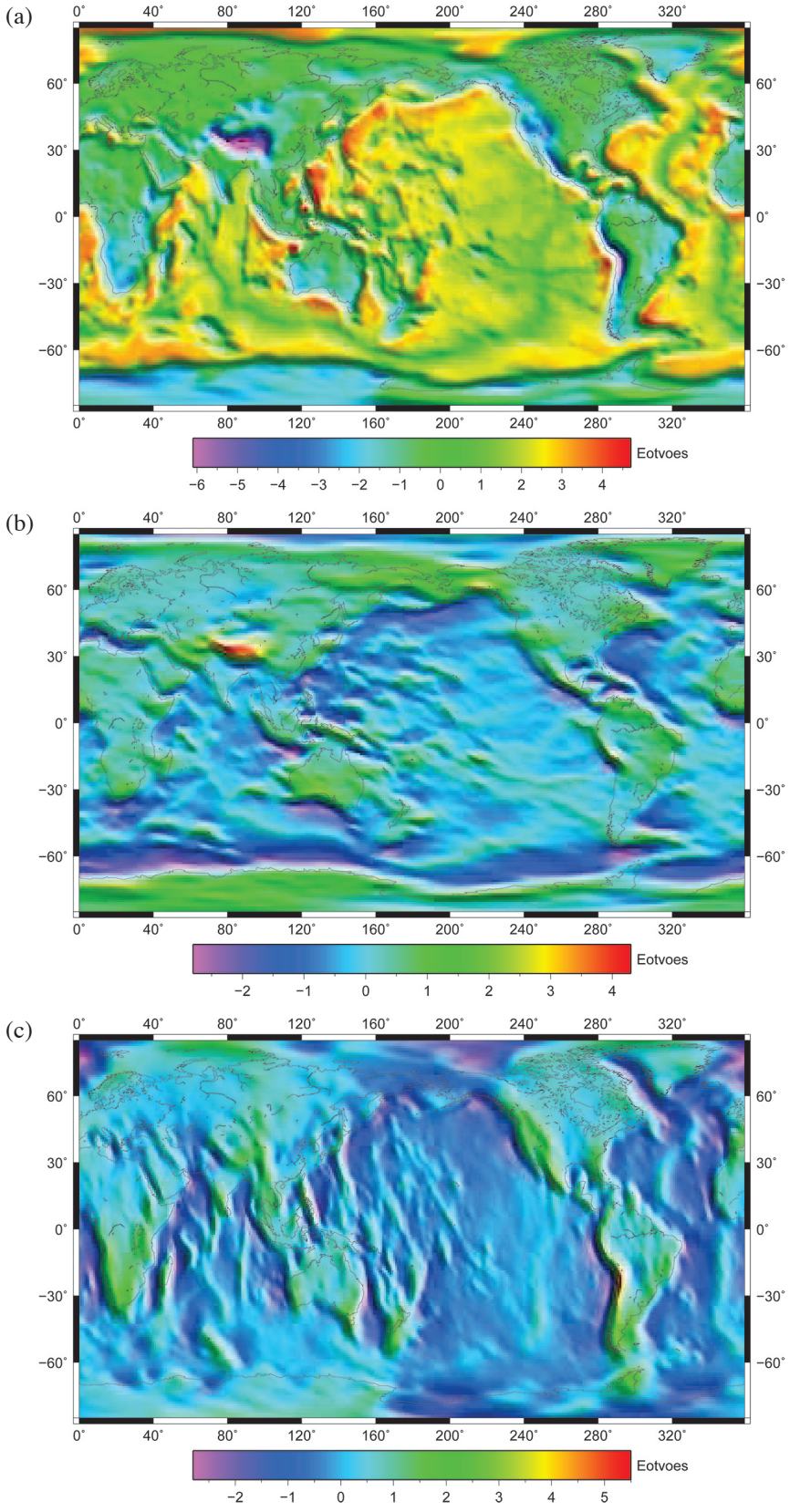

Fig. 4. The topography-corrected and bathymetry- and ice-stripped gravity gradient components: Γ_{rr}^{tbi} (a), $\Gamma_{\phi\phi}^{tbi}$ (b) and $\Gamma_{\lambda\lambda}^{tbi}$ (c) computed globally on a one arc-deg grid at a mean satellite elevation of 255 km using the GOCO-03s, DTM2006 and ice-thickness coefficients including ice thickness data. Values are in E (= 10^{-9} s^{-2}).

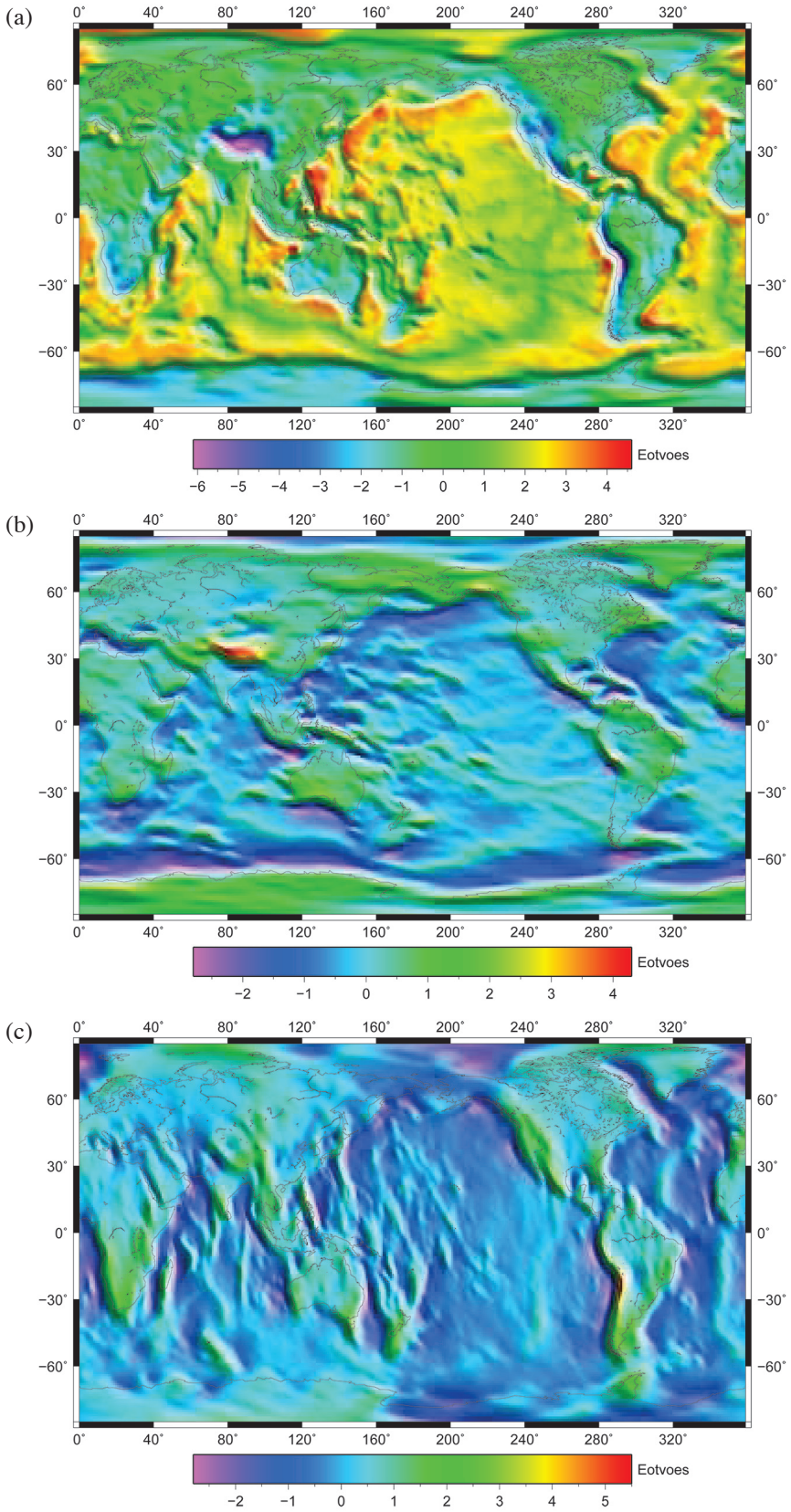

Fig. 5. The topography-corrected and bathymetry-, ice- and sediment-stripped gravity gradient components: Γ_{rr}^{tbis} (a), $\Gamma_{\phi\phi}^{tbis}$ (b) and $\Gamma_{\lambda\lambda}^{tbis}$ (c) computed globally on a one arc-deg surface grid at a mean satellite elevation of 255 km using the GOCO-03s, DTM2006 and ice-thickness coefficients and the CRUST2.0 sediment coefficients. Values are in E (= 10^{-9} s^{-2}).

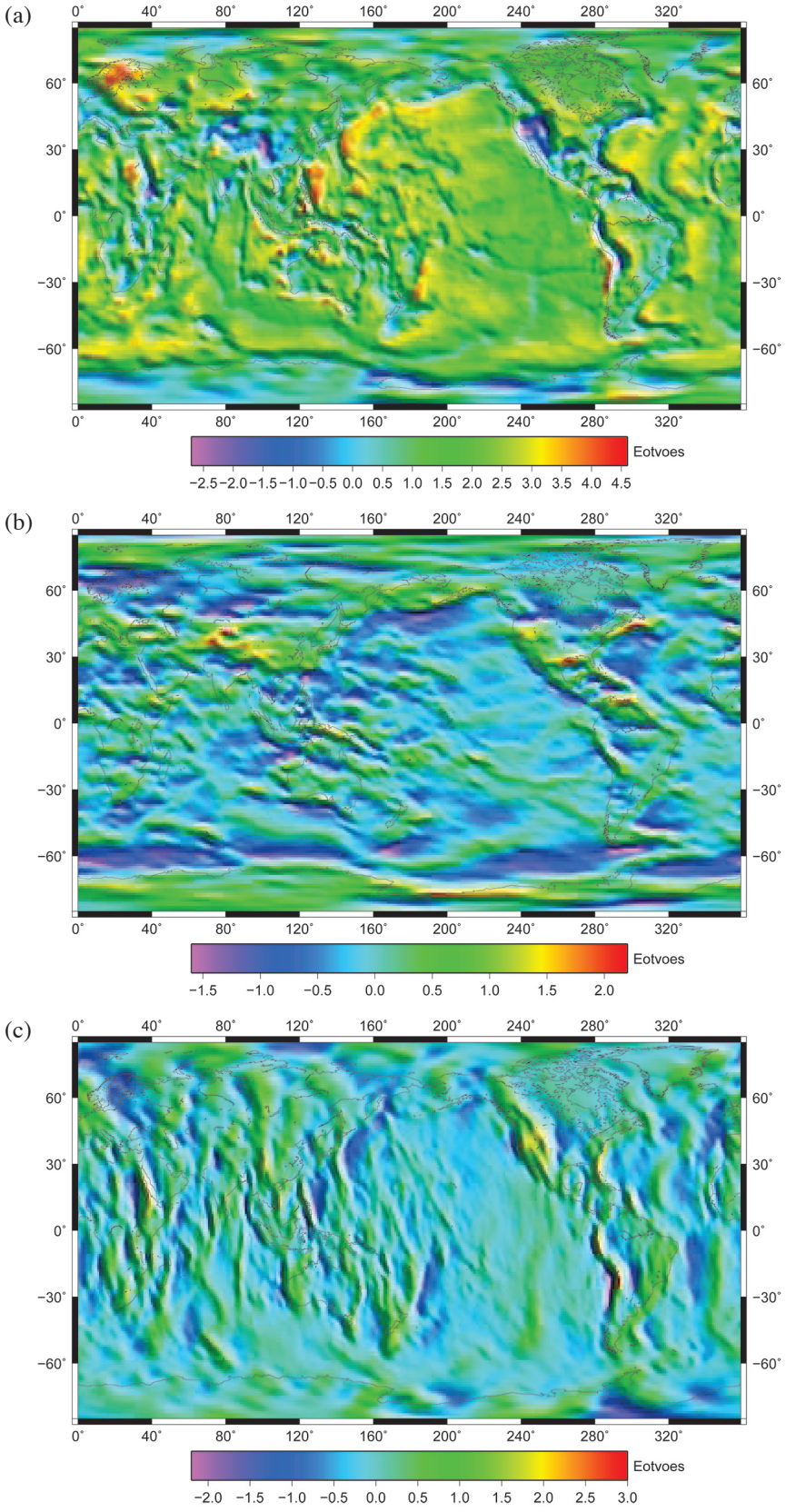

Fig. 6. The consolidated crust-stripped gravity gradient components: Γ^{cs}_{rr}(a), $\Gamma^{cs}_{\phi\phi}$(b) and $\Gamma^{cs}_{\lambda\lambda}$(c) computed globally on a one arc-deg surface grid at the mean satellite elevation of 255 km using the GOCO-03s, DTM2006 and ice-thickness coefficients and the CRUST2.0 sediment and consolidated crust coefficients. Values are in E (= 10^{-9} s^{-2}).

ocean, ice, sediments and between crustal layers. These corrections were then applied to diagonal components of the Marussi gravity gradient tensor. The topographic density of 2670 kg m^{-3} was used to compute topographic correction. The same value of the reference crustal density was adopted to define the density contrasts within the remaining crust below sea level down to the Moho. The gravity gradient components and respective corrections were computed based on methods for a spherical harmonic analysis and synthesis of the gravity field. The numerical results of the stepwise corrected gravity gradients were presented globally on a one arc-deg grid at a mean satellite elevation of 255 km.

The application of topographic and stripping corrections due to density contrasts of the ocean, ice, sediments and between crustal layers substantially changed the gravity gradient field (Figs. 1 - 6). Compared to a relatively smooth pattern of the Earth's gravity gradient field (Fig. 1), the consolidated crust-stripped gravity gradient field is characterized by large spatial variations (Fig. 6). The maximum spatial variations in the (refined) gravity gradient field correspond with the largest lateral changes of the Moho geometry and lithospheric structures, especially at more shallow depths. The most significant features observed in the refined gravity gradient field over oceans are attributed to heterogeneous structures of the oceanic lithosphere caused by mantle convection. In particular, the oceanic, divergent tectonic plate boundaries (along the mid-oceanic rift zones) and oceanic subduction zones are well pronounced. The signature of the divergent tectonic plate boundaries is further extended along continental rift zones. Elsewhere over continents, the most pronounced features in the gravity gradient field are related to continental lithospheric thickness and glacial isostatic rebound. The global tectonic configuration is distinctly marked along the continental margins revealing the contrast between different crustal thicknesses and lithospheric composition of the oceanic and continental lithosphere.

The application of topographic and stripping gravity corrections, due to all known anomalous crustal density structures to a gravity field revealed the signature of the Moho geometry. Consequently, the application of these corrections to the gravity gradient field revealed spatial variations of the Moho geometry. Moreover, the refined gravity and gravity gradient field also comprise the signals of the mantle lithosphere and sub-lithospheric mantle down to the core-mantle boundary. The signature of these deeper sources is, however, much less pronounced in the gravity gradient field. Large uncertainties in both gravity data types are mainly due to low accuracy and poor resolution of the CRUST2.0 sediment and crustal layer data. The computation of the topographic and stripping corrections of the ocean and ice density contrasts is more accurate. The improved accuracy of computed gravity gradients was achieved using GOCO-03s.

Gravity data are the most commonly used in gravimetric studies investigating lithospheric structure. Conversely, the application of gravity gradients in these studies has previously been relatively rare. In this study we compiled a global gravity gradient dataset which can be used to study the Moho density contrast. The geophysical interpretation of the gravity gradient field should also improve the resolution of other lithospheric structures, especially localized information. Our results revealed that the signature of shallower density structures within the Earth's crust is well recognized in the (refined) gravity gradient field. The application of the gravity gradient field is thus very promising especially for a gravimetric interpretation of shallow lithospheric structures, because the signal from deeper sources quickly attenuates compared to gravity or potential fields. The gravity gradients can thus provide additional constraining information to enhance more commonly used geophysical exploration methods such as seismic tomography.

Acknowledgements Pavel Novák was supported by the Czech Science Foundation, project 209/12/1929. This research was financially supported by the Chinese Ministry of Education.

REFERENCES

Artemjev, M. E., M. K. Kaban, V. A. Kucherinenko, G. V. Demyanov, and V. A. Taranov, 1994: Subcrustal density inhomogeneities of Northern Eurasia as derived from the gravity data and isostatic models of the lithosphere. *Tectonophysics,* **240**, 249-280, doi: 10.1016/0040-1951(94)90275-5. [Link]

Bagherbandi, M. and L. E. Sjöberg, 2012: Non-isostatic effects on crustal thickness: A study using CRUST2.0 in Fennoscandia. *Phys. Earth Planet. Inter.*, **200-201**, 37-44, doi: 10.1016/j.pepi.2012.04.001. [Link]

Bassin, C., G. Laske, and G. Masters, 2000: The current limits of resolution for surface wave tomography in North America. *Eos, Trans., AGU*, **81**, F897.

Braitenberg, C., S. Wienecke, and Y. Wang, 2006: Basement structures from satellite-derived gravity field: South China Sea ridge. *J. Geophys. Res.*, **111**, B05407, doi: 10.1029/2005JB003938. [Link]

Cutnell, J. D. and K. W. Johnson, 1995: Physics, 3rd Edition, Wiley, New York.

Ditmar, P. and R. Klees, 2002: A Method to Compute the Earth's Gravity Field from SGG/SST Data to be Acquired by the GOCE Satellite. DUP Science, Delft University Press, Delft, The Netherlands, 64 pp.

Ekholm, S., 1996: A full coverage, high-resolution, topographic model of Greenland computed from a variety of digital elevation data. *J. Geophys. Res.*, **101**, 21961-21972, doi: 10.1029/96JB01912. [Link]

Förste, C., R. Schmidt, R. Stubenvoll, F. Flechtner, U. Meyer, R. König, H. Neumayer, R. Biancale, J.-M.

Lemoine, S. Bruinsma, S. Loyer, F. Barthelmes, and S. Esselborn, 2008: The GeoForschungsZentrum Potsdam/Groupe de Recherche de Gèodésie Spatiale satellite-only and combined gravity field models: EIGEN-GL04S1 and EIGEN-GL04C. *J. Geodesy*, **82**, 331-346, doi: 10.1007/s00190-007-0183-8. [Link]

Gladkikh, V. and R. Tenzer, 2012: A mathematical model of the global ocean saltwater density distribution. *Pure Appl. Geophys.*, **169**, 249-257, doi: 10.1007/s00024-011-0275-5. [Link]

Goiginger, H., D. Rieser, T. Mayer-Gürr, R. Pail, T. Fecher, T. Gruber, A. Albertella, A. Maier, E. Höck, S. Krauss, W. Hausleitner, O. Baur, A. Jäggi, U. Meyer, J. M. Brockmann, W.-D. Schuh, I. Krasbutter, and J. Kusche, 2001: GOCO, Consortium: The satellite-only global gravity field model GOCO02S. European Geosciences Union General Assembly 2011, Vienna, 04.04.2011.

Gouretski, V. V. and K. P. Koltermann, 2004: WOCE Global Hydrographic Climatology, Berichte des Bundesamtes für Seeschifffahrt und Hydrographie, Nr. 35.

Hammer, S., 1963: Deep gravity interpretation by stripping. *Geophysics*, **28**, 369-378, doi: 10.1190/1.1439186. [Link]

Hinze, W., 2003: Bouguer reduction density, why 2.67? *Geophysics*, **68**, 5, 1559-1560, doi: 10.1190/1.1620629. [Link]

Johnson, D. R., H. E. Garcia, and T. P. Boyer, 2009: World ocean database 2009 tutorial. In: Levitus, S. (Ed.), National Oceanographic Data Center Internal Report 21, NOAA Printing Office, Silver Spring, Maryland, October 18, 2009, 18 pp.

Kaban, M. K., P. Schwintzer, and S. A. Tikhotsky, 1999: A global isostatic gravity model of the Earth. *Geophys. J. Int.*, **136**, 519-536, doi: 10.1046/j.1365-246x.1999.00731.x. [Link]

Kaban, M. K., P. Schwintzer, I. M. Artemieva, and W. D. Mooney, 2003: Density of the continental roots: Compositional and thermal contributions. *Earth Planet. Sci. Lett.*, **209**, 53-69, doi: 10.1016/S0012-821X(03)00072-4. [Link]

Kaban, M. K., P. Schwintzer, and C. Reigber, 2004: A new isostatic model of the lithosphere and gravity field. *J. Geodesy*, **78**, 368-385, doi: 10.1007/s00190-004-0401-6. [Link]

Lythe, M. B. and D. G. Vaughan, 2001: BEDMAP: A new ice thickness and subglacial topographic model of Antarctica. *J. Geophys. Res.*, **106**, 11335-11351, doi: 10.1029/2000JB900449. [Link]

Mayer-Gürr, T., R. Pail, T. Gruber, T. Fecher, M. Rexer, W.-D. Schuh, J. Kusche, J.-M. Brockmann, I. Krasbutter, S. Becker, A. Eicker, J. Schall, D. Rieser, N. Zehentner, O. Baur, E. Höck, W. Hausleitner, A. Maier, S. Krauss, A. Jäggi, U. Meyer, and L. Prange, 2012: The new combined satellite only model GOCO03s. International Symposium on Gravity, Geoid and Height Systems 2012, Venice, Italy.

Moritz, H., 2000: Geodetic reference system 1980. *J. Geodesy*, **74**, 128-133, doi: 10.1007/s001900050278. [Link]

Negretti, M., M. Reguzzoni, and D. Sampietro, 2012: A Web Processing Service for GOCE data exploitation. First International GOCE Solid Earth Workshop, 16-17 October 2012, Enschede, The Netherlands.

Novák, P., 2010: High resolution constituents of the Earth's gravitational field. *Surv. Geophys.*, **31**, 1-21, doi: 10.1007/s10712-009-9077-z. [Link]

Pail, R., S. Bruinsma, F. Migliaccio, C. Förste, H. Goiginger, W.-D. Schuh, E. Höck, M. Reguzzoni, J. M. Brockmann, O. Abrikosov, M. Veicherts, T. Fecher, R. Mayrhofer, I. Krasbutter, F. Sansò, N. K. Pavlis, J. K. Factor, and S. A. Holmes, 2007: Terrain-related gravimetric quantities computed for the next EGM. In: Kilicoglu, A. and R. Forsberg (Eds.), Gravity Field of the Earth, Proceedings of the 1st International Symposium of the International Gravity Field Service (IGFS), Harita Dergisi, Special Issue, No. 18, General Command of Mapping, Ankara, Turkey.

Pavlis, N. K., S. A. Holmes, S. C. Kenyon, and J. K. Factor, 2012: The development and evaluation of the Earth Gravitational Model 2008 (EGM2008). *J. Geophys. Res.*, **117**, B04406, doi: 10.1029/2011JB008916. [Link]

Sampietro, D., M. Reguzzoni, and C. Braitenberg, 2013: The GOCE estimated Moho beneath the Tibetan Plateau and Himalaya. In: Rizos, C. and P. Willis (Eds.), International Association of Geodesy Symposia, Earth on the Edge: Science for a Sustainable Planet, Proceedings of the IAG General Assembly, 28 June - 2 July 2011, Melbourne, Australia, Vol. 139, Springer-Verlag, Berlin.

Simmons, N. A., A. M. Forte, L. Boschi, and S. P. Grand, 2010: GyPSuM: A joint tomographic model of mantle density and seismic wave speeds. *J. Geophys. Res.*, **115**, B12310, doi: 10.1029/2010JB007631. [Link]

Sjöberg, L. E. and M. Bagherbandi, 2011: A method of estimating the Moho density contrast with a tentative application of EGM08 and CRUST2.0. *Acta Geophys.*, **59**, 502-525, doi: 10.2478/s11600-011-0004-6. [Link]

Tenzer, R., K. Hamayun, and P. Vajda, 2009a: Global maps of the CRUST2.0 crustal components stripped gravity disturbances. *J. Geophys. Res.*, **114**, B05408, doi: 10.1029/2008JB006016. [Link]

Tenzer, R., Hamayun, and P. Vajda, 2009b: A global correlation of the step-wise consolidated crust-stripped gravity field quantities with the topography, bathymetry, and the CRUST 2.0 Moho boundary. *Contrib. Geophys. Geod.*, **39**, 133-147, doi: 10.2478/v10126-009-0006-4. [Link]

Tenzer, R., A. Abdalla, P. Vajda, and Hamayun, 2010: The spherical harmonic representation of the gravitational

field quantities generated by the ice density contrast. *Contrib. Geophys. Geod.*, **40**, 207-223, doi: 10.2478/v10126-010-0009-1. [Link]

Tenzer, R., P. Novák, and V. Gladkikh, 2011: On the accuracy of the bathymetry-generated gravitational field quantities for a depth-dependent seawater density distribution. *Stud. Geophys. Geod.*, **55**, 609-626, doi: 10.1007/s11200-010-0074-y. [Link]

Tenzer, R., P. Novák, P. Vajda, V. Gladkikh, and Hamayun, 2012a: Spectral harmonic analysis and synthesis of Earth's crust gravity field. *Comput. Geosci.*, **16**, 193-207, doi: 10.1007/s10596-011-9264-0. [Link]

Tenzer, R., V. Gladkikh, P. Novák, and P. Vajda, 2012b: Spatial and spectral analysis of refined gravity data for modelling the crust-mantle interface and mantle-lithosphere structure. *Surv. Geophys.*, **33**, 817-839, doi: 10.1007/s10712-012-9173-3. [Link]

Tenzer, R., P. Novák, and V. Gladkikh, 2012c: The bathymetric stripping corrections to gravity field quantities for a depth-dependent model of seawater density. *Mar. Geodesy*, **35**, 198-220, doi: 10.1080/01490419.2012.670592. [Link]

Watts, A. B., 2001: Isostasy and Flexure of the Lithosphere. Cambridge University Press, Cambridge, New York, 480 pp.

Wienecke, S., C. Braitenberg, and H.-J. Götze, 2007: A new analytical solution estimating the flexural rigidity in the Central Andes. *Geophys. J. Int.*, **169**, 789-794, doi: 10.1111/j.1365-246X.2007.03396.x. [Link]

APPENDIX A: GRAVIMETRIC FORWARD MODELING

Tenzer et al. (2012a) developed and applied a uniform mathematical formalism of computing the gravity corrections. It utilizes the expression for the gravitational potential V generated by an arbitrary volumetric mass layer with a variable depth and thickness while having laterally distributed vertical mass density variations. For a computation point (r, Ω),

$$V(r,\Omega) = \frac{GM}{R} \sum_{n=0}^{\bar{n}} \sum_{m=-n}^{n} \left(\frac{R}{r}\right)^{n+1} V_{n,m}\, Y_{n,m}(\Omega) \tag{A1}$$

where $GM = 3986005 \times 10^8$ m^3 s^{-2} is the geocentric gravitational constant, $R = 6371 \times 10^3$ m is the Earth's mean radius, $Y_{n,m}$ is the surface spherical harmonic functions of degree n and order m and $V_{n,m}$ are potential coefficients. $\bar{n}$ is the maximum degree of spherical harmonics. The 3-D position is defined in the system of geocentric spherical coordinates (r,Ω); where, r is the geocentric radius, and $\Omega = (\phi, \lambda)$ denotes the geocentric direction with the spherical latitude ϕ and longitude λ. The potential coefficients $V_{n,m}$ in Eq. (A1) are defined as

$$V_{n,m} = \frac{3}{2n+1} \frac{1}{\bar{\rho}^{\,\mathrm{Earth}}} \sum_{i=0}^{I} \left(Fl_{n,m}^{(i)} - Fu_{n,m}^{(i)}\right) \tag{A2}$$

where $\bar{\rho}^{\,\mathrm{Earth}} = 5500$ kg m^{-3} is the adopted value of the Earth's mean mass density (cf. Novák 2010). The numerical coefficients $\{Fl_{n,m}^{(i)}, Fu_{n,m}^{(i)} : i = 0, 1, ..., I\}$ are given by

$$Fl_{n,m}^{(i)} = \sum_{k=0}^{n+2} \binom{n+2}{k} \frac{(-1)^k}{k+1+i} \frac{L_{n,m}^{(k+1+i)}}{R^{k+1}} \tag{A3}$$

and

$$Fu_{n,m}^{(i)} = \sum_{k=0}^{n+2} \binom{n+2}{k} \frac{(-1)^k}{k+1+i} \frac{U_{n,m}^{(k+1+i)}}{R^{k+1}} \tag{A4}$$

The terms $\sum_{m=-n}^{n} L_{n,m} Y_{n,m}$ and $\sum_{m=-n}^{n} U_{n,m} Y_{n,m}$ define the spherical lower and upper-bounds of laterally distributed radial density variation functions L_n and U_n of degree n. These numerical coefficients combine information on the geometry and mass density (or mass density contrast) distribution within the volumetric layer. The computation of these coefficients reveals a certain degree of spherical harmonics using discrete data of the spatial mass density distribution (typically provided by density, depth and thickness data) of a particular structural component of the Earth's interior. The spherical functions L_n, U_n and their higher-order terms $\{L_n^{(k+1+i)}, U_n^{(k+1+i)} : k = 0, 1, ...; i = 1, 2, ..., I\}$ are computed using the following expressions

$$L_n^{(k+1+i)}(\Omega) = \begin{cases} \dfrac{4\pi}{2n+1} \iint_{\Phi} \rho(D_U, \Omega')\, D_L^{k+1}(\Omega')\, P_n(\cos\psi)\, d\Omega' \\ = \sum_{m=-n}^{n} L_{n,m}^{(k+1)}\, Y_{n,m}(\Omega), \quad i = 0 \\ \dfrac{4\pi}{2n+1} \iint_{\Phi} \beta(\Omega')\, a_i(\Omega')\, D_L^{k+1+i}(\Omega') \\ \cdot P_n(\cos\psi)\, d\Omega' = \sum_{m=-n}^{n} L_{n,m}^{(k+1+i)}\, Y_{n,m}(\Omega), \\ i = 1, 2, ..., I \end{cases} \tag{A5}$$

and

$$U_n^{(k+1+i)}(\Omega) = \begin{cases} \dfrac{4\pi}{2n+1} \iint_{\Phi} \rho(D_U, \Omega')\, D_U^{k+1}(\Omega')\, P_n(\cos\psi)\, d\Omega' \\ = \sum_{m=-n}^{n} U_{n,m}^{(k+1)}\, Y_{n,m}(\Omega), \quad i = 0 \\ \dfrac{4\pi}{2n+1} \iint_{\Phi} \beta(\Omega')\, a_i(\Omega')\, D_U^{k+1+i}(\Omega') \\ \cdot P_n(\cos\psi)\, d\Omega' = \sum_{m=-n}^{n} U_{n,m}^{(k+1+i)}\, Y_{n,m}(\Omega), \\ i = 1, 2, ..., I \end{cases} \tag{A6}$$

Where P_n are the Legendre polynomials of degree n, and ψ is the spherical distance between two points (r, Ω) and (r', Ω').

The depths D_U and D_L of the upper-bound and lower-bound of the volumetric mass density layer are defined with respect to a sphere of radius R. The infinitesimal surface element on the unit sphere is denoted as $d\Omega' = \cos\phi'\, d\phi'\, d\lambda'$, and $\Phi = \{\Omega' = (\phi', \lambda') : \phi' \in [-\pi/2, \pi/2] \wedge \lambda' \in [0, 2\pi)\}$ is the full spatial angle. For a specific volumetric layer, the mass density ρ is either constant ρ, laterally-varying $\rho(\Omega')$ or, in the most general case, approximated by the laterally distributed radial density variation model using the following polynomial function (for each lateral column)

$$\begin{aligned} &\rho(r', \Omega') = \rho(D_U, \Omega') + \beta(\Omega') \sum_{i=1}^{I} a_i(\Omega')(\mathrm{R} - r')^i, \\ &for \quad \mathrm{R} - D_U(\Omega') \geq r' > \mathrm{R} - D_L(\Omega') \end{aligned} \tag{A7}$$

The nominal value of the lateral density $\rho(D_U, \Omega')$ is defined at depth D_U. This density distribution model describes the radial density variation (by means of the coefficients $\{\alpha : i = 1, 2, ..., I\}$ and β) within the volumetric mass layer at a location Ω'. Alternatively, when modeling the gravitational field of anomalous density structures, the density contrast $\Delta\rho$ of the volumetric mass layer relative to the reference density ρ^c is defined as

$$\begin{aligned} \Delta\rho(r', \Omega') &= \rho^c - \rho(r', \Omega') \\ &= \Delta\rho(D_U, \Omega') - \beta(\Omega') \sum_{i=1}^{I} a_i(\Omega')(\mathrm{R} - r')^i, \\ &\quad for \quad \mathrm{R} - D_U(\Omega') \geq r' > \mathrm{R} - D_L(\Omega') \end{aligned} \tag{A8}$$

where $\Delta\rho(D_U, \Omega')$ is the nominal value of the lateral density contrast at depth D_U. Here the reference density ρ^c of a homogenous crust is used.

APPENDIX B: DIAGONAL GRAVITY GRADIENT COMPONENTS

The spectral representation of V in Eq. (A1) in terms of the potential coefficients $V_{n,m}$ [Eq. (A2)] is utilized here to compute the corrections to the diagonal components Γ_{rr}, $\Gamma_{\phi\phi}$ and $\Gamma_{\lambda\lambda}$ of the Marussi gravitational gradient (second-order) tensor (e.g., Ditmar and Klees 2002):

$$\begin{aligned} &\Gamma_{rr} \equiv V_{rr} = \frac{\partial^2 V}{\partial r^2}, \quad \Gamma_{\phi\phi} = \frac{1}{r^2} V_{\phi\phi} = \frac{1}{r^2} \frac{\partial^2 V}{\partial \phi^2}, \\ &\Gamma_{\lambda\lambda} = \frac{1}{r^2 \cos^2\phi} V_{\lambda\lambda} = \frac{1}{r^2 \cos^2\phi} \frac{\partial^2 V}{\partial \lambda^2} \end{aligned} \tag{B1}$$

The second-order partial derivatives of V with respect to the spherical coordinates (r, ϕ, λ) in Eq. (B1) are given by Ditmar and Klees (2002):

$$\frac{\partial^2 V}{\partial r^2} = \frac{\mathrm{GM}}{\mathrm{R}^3} \sum_{n=0}^{\bar{n}} \sum_{m=-n}^{n} \left(\frac{\mathrm{R}}{r}\right)^{n+3} (n+1)(n+2) \mathrm{V}_{n,m}\, \mathrm{Y}_{n,m}(\Omega) \tag{B2}$$

$$\frac{\partial^2 V}{\partial \phi^2} = \frac{\mathrm{GM}}{\mathrm{R}} \sum_{n=0}^{\bar{n}} \sum_{m=-n}^{n} \left(\frac{\mathrm{R}}{r}\right)^{n+1} \frac{\partial^2 \mathrm{Y}_{n,m}(\Omega)}{\partial \phi^2} \mathrm{V}_{n,m} \tag{B3}$$

$$\frac{\partial^2 V}{\partial \lambda^2} = -\frac{\mathrm{GM}}{\mathrm{R}} \sum_{n=0}^{\bar{n}} \sum_{m=-n}^{n} \left(\frac{\mathrm{R}}{r}\right)^{n+1} m^2\, \mathrm{Y}_{n,m}(\Omega)\, \mathrm{V}_{n,m} \tag{B4}$$